NANO LETTERS

pubs.acs.org/NanoLett

Letter

Magnetic Vortex States in Toroidal Iron Oxide Nanoparticles: Combining Micromagnetics with Tomography

George R. Lewis, James C. Loudon, Robert Tovey, Yen-Hua Chen, Andrew P. Roberts, Richard J. Harrison, Paul A. Midgley, and Emilie Ringe*

Cite This: https://dx.doi.org/10.1021/acs.nanolett.0c02795

Read Online

ACCESS | Metrics & More | Article Recommendations | Supporting Information

ABSTRACT: Iron oxide nanorings have great promise for biomedical applications because of their magnetic vortex state, which endows them with a low remanent magnetization while retaining a large saturation magnetization. Here we use micromagnetic simulations to predict the exact shapes that can sustain magnetic vortices, using a toroidal model geometry with variable diameter, ring thickness, and ring eccentricity. Our model phase diagram is then compared with simulations of experimental geometries obtained by electron tomography. High axial eccentricity and low ring thickness are found to be key factors for forming vortex states and avoiding net-magnetized metastable states. We also find that while defects from a perfect toroidal geometry increase the stray field associated with the vortex state, they can also make the vortex state more energetically accessible. These results constitute an important step toward optimizing the magnetic behavior of toroidal iron oxide nanoparticles.

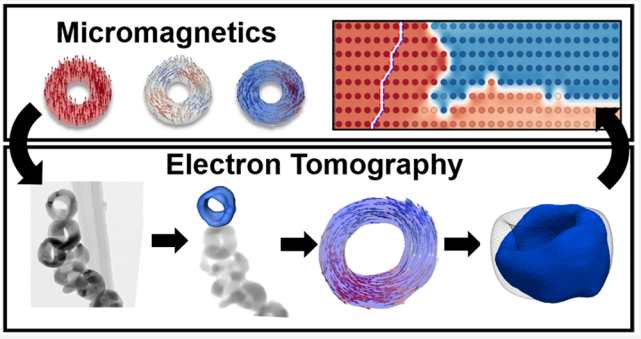

KEYWORDS: *Iron Oxide Nanoparticles, Vortex, Micromagnetics, Tomography, TEM*

Toroidal magnetic nanoparticles (NPs) can sustain high net saturation magnetization in high fields with minimal remanent magnetization in low fields. This is enabled by the presence of a vortex state of circulating magnetization at low fields. This "on/off" switching property is of interest for the biomedical applications of iron oxide NPs that benefit from biocompatibility and magnetic properties,[1−3] with the magnetite phase being key due to its large saturation magnetization[4] (Supporting Information (SI)). Superparamagnetic iron oxide NPs have been explored for hyperthermic cancer therapy,[5,6] targeted drug-delivery,[7] and MRI contrast agents[8] because their on/off switching capability enables agglomeration-free dispersions in the absence of an external magnetic field. However, progress has been limited by the relatively weak response to magnetic fields (i.e., low saturation magnetization) that stems from their extremely small size.[9]

Control over the shape and size of iron oxide NPs enables manipulation of their physical properties; various morphologies, including spheres, rods, plates, cubes, hexagons, disks, tubes, and rings, exist with sizes from five to several hundred nanometers.[10−14] Of these shapes, the toroidal rings and tubes are uniquely able to sustain a closed-flux magnetic vortex remanent state because the central cavity allows these geometries to avoid the formation of a vortex core where the magnetization is forced to rotate out-of-plane and produce stray fields in nontoroidal shapes.[15] This enables toroids to display the on/off magnetic switching characteristic of superparamagnetism but with larger NPs and stronger magnetic responses (SI Figure S1). These NPs are typically made via hydrothermal synthesis,[13,16,17] and demonstrated promising results with both *in vitro*[18] and *in vivo* studies[19−22] for hyperthermia, as well as for photocatalysts,[23] lithium battery anodes,[24] and electromagnetic wave absorbers.[25,26]

The vortex state involves a circulating magnetization in NPs that are too large to remain uniformly magnetized but without sufficient demagnetizing effects to become multidomain. Previous investigations show that rings can also adopt an out-of-plane magnetization state and an "onion state"[27] (a net in-plane magnetized state where spins curl around the ring in two symmetric halves). Experimental and simulated phase diagrams show that out-of-plane remanent states form for tall, low diameter rings, onion states form in short rings, and vortex states form for tall, large diameter rings,[18,28−30] similar to the phase diagrams for magnetic disks,[31,32] plates,[33] and ellipsoids.[34] Investigations into the impact of realistic shape

Received: July 6, 2020
Revised: September 11, 2020
Published: September 11, 2020

imperfections have been limited. Existing micromagnetic simulations of nanoring phase diagrams all use finite domain simulations of perfectly cylindrical particles, which are suited to the well-defined geometries obtained through electron-beam/nanoimprint lithography, yet fail to capture the curvature typically present in colloidal samples. Systematic studies of asymmetric particles include the analysis of artificially notched rings/disks,[28,35] slotted rings[36] and spheres with conical bumps,[37] but no simulated studies use real ring geometries although the experiments of Eltschka et al. demonstrate a correlation between experimental geometry and magnetization configuration[38] deserving further exploration. Furthermore, much of the literature in this area focuses on permalloy, nickel, cobalt, and pure iron particles in thin-film geometries geared toward switching mechanisms and vortex chirality for application in memory devices,[27,39−43] rather than toward the remanent state behavior in magnetite NPs for biomedical applications.

Here, we address this knowledge gap by numerically and experimentally investigating the vortex state in toroidal magnetite NPs. We use finite element micromagnetics to simulate a magnetic phase diagram that predicts the remanent state for toroidal NP geometries and use experimental geometries from electron tomography to simulate realistic remanent magnetization states which enables comparison to the phase diagram. We subsequently use the tomographic shape to analyze the impact of deviations from the ideal toroid shape on the magnetic behavior of the NPs.

NANOPARTICLE STRUCTURE AND COMPOSITION

Toroidal iron oxide NPs prepared via a hydrothermal synthesis route[11,44,45] (Supporting Information) showed mostly ring-shapes with typical diameters of 60−90 nm and 15−30 nm ring widths. Scanning transmission electron microscopy energy-dispersive X-ray spectroscopy (STEM-EDX) mapping of the O and Fe K_α peaks confirmed that the sample contains Fe and O (Figure 1). The carbon reduction synthetic approach produces magnetite (Fe_3O_4),[11,44,45] however, magnetite NPs stored in air at room temperature partially oxidize to maghemite (γ-Fe_2O_3) over several weeks,[46] such that our NPs are likely a magnetite/maghemite mixture (Supporting Information). First-order reversal curve (FORC) measurements suggest that the sample contains a mixture of predominantly vortex states with minor onion state and single domain contributions (SI Figure S2).

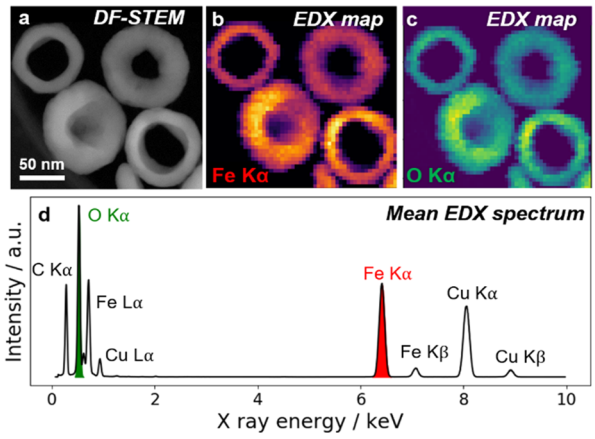

Figure 1. Elemental composition of toroidal iron oxide NPs. (a) HAADF-STEM image, (b, c) elemental maps from the integrated, background subtracted Fe K_α and O K_α peaks. (d) Mean EDX spectrum. The C and Cu signals result from the C/Cu supporting grid.

MAGNETIC PHASE DIAGRAM

Magnetic phase diagrams for toroidal magnetite NPs were simulated using MERRILL,[47] an open source finite element micromagnetic simulator well-suited for irregular shapes. The toroidal shapes are mathematically formed by revolution of an ellipse along an axis parallel to its semimajor axis with radius of rotation R. Three shape parameters were explored based on experimentally observed variations: ring thickness r/R, defined as the ratio of the semiminor ellipse axis r to radius of rotation R; total ring diameter d_{tot} ($2r + 2R$); and elliptical eccentricity e (SI Figure S3). For each geometry, the remanent magnetization state was found as a local minimum in the total micromagnetic energy E_{tot} from several initial magnetization states (uniform x, uniform y, uniform z, and five different random configurations), and the net magnetization magnitude M/M_S was calculated. Two data sets were subsequently extracted at each geometry: the state with the lowest E_{tot}, and that with the highest M/M_S (corresponding to a probable ground state and potential metastable state, respectively).

The magnetic state of iron oxide toroids depends strongly on their shape. The phase diagram for each eccentricity value is broadly split into three regions when considering high M/M_S states: small diameter NPs ($\lesssim$120 nm) have single domain behavior, and large diameter NPs ($\gtrsim$120 nm) form onion states when thin ($r/R \lesssim 0.4$) or vortex states when thick ($r/R \gtrsim 0.4$) (Figure 2). Three-region phase diagrams have been previously observed[28,29,32,33] but with the notable difference that M/M_S does not easily distinguish between in-plane or out-of-plane magnetization. Additional analyses confirm that more tubular rings prefer out-of-plane behavior, whereas lower eccentricity ones are likely to have in-plane magnetization (SI Figure S4).

When considering the low E_{tot} data set (ground states) for each geometry, the phase diagram splits into just two regions with single domain behavior at small d_{tot} and vortex behavior at large d_{tot} (dashed lines, Figure 2). To validate that vortex states are the ground state for high d_{tot} NPs, remanent states were calculated from 1000 random initial states for a typical NP geometry with convincing results (SI Figure S5). The lack of a third region suggests that the onion state is only a local energy minimum for geometries that would otherwise form the vortex state. This also suggests that the region d_{tot} from $\sim$ 60 nm to $\sim$130 nm (depending on r/R and e) is a large transition region where both onion and vortex states can form with the energetically favored state being the vortex state. This concurs with a recent study on permalloy rings where the vortex state was more stable for all tested geometries.[43] Toroidal NPs in the transition region could thus potentially be coaxed into the vortex state given enough energy to overcome the reconfiguration barrier. Calculated minimum energy pathways for a typical NP (d_{tot} 70 nm, r/R 0.4, and e 0.7) suggest that the uniform z metastable state is particularly unstable (SI Figure S6).

The minimum size at which the vortex state forms varies from 50 to 70 nm depending on NP geometry (dashed lines in Figure 2). This is rationalized by comparison to the 61 nm single to multidomain transition in cubic magnetite NPs[48] and is consistent with simulations of hollow magnetite cylinders where the smallest vortex state was observed at 60 nm.[28] It also

https://dx.doi.org/10.1021/acs.nanolett.0c02795
Nano Lett. XXXX, XXX, XXX−XXX

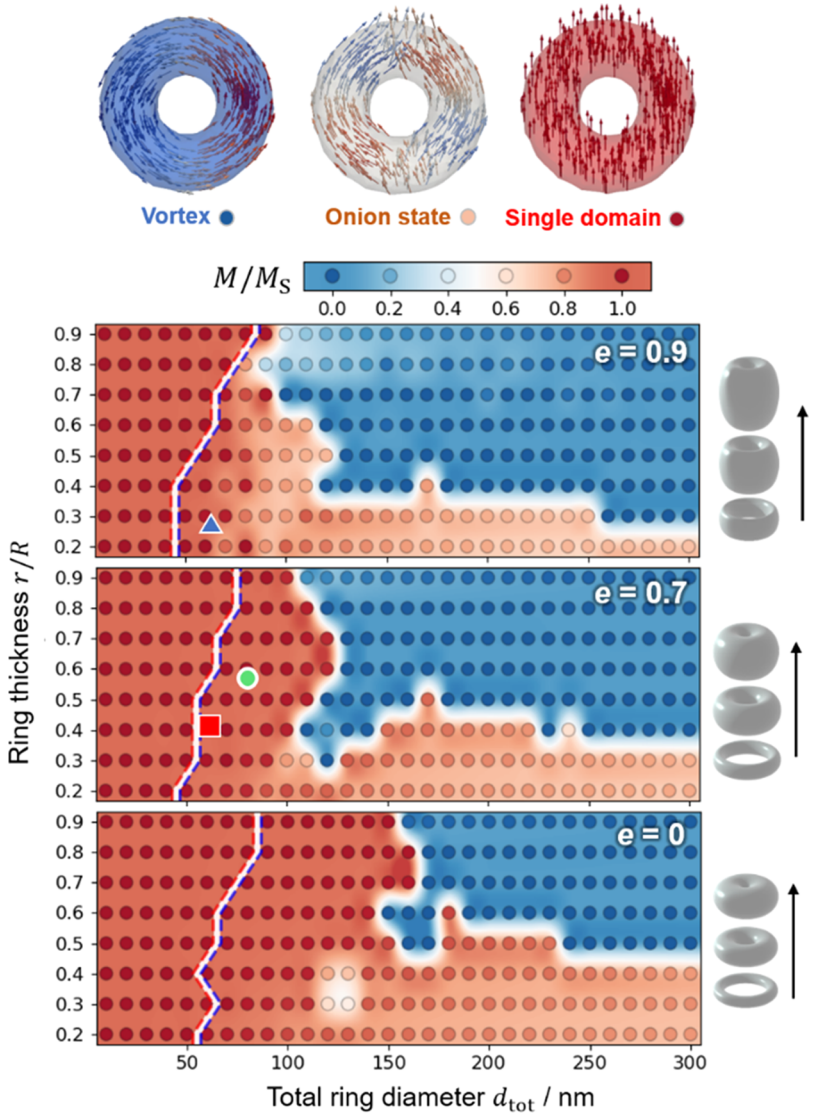

Figure 2. Magnetic phase diagram. Magnetic remanent states for micromagnetic simulations of magnetite toroids at varying ring size d_{tot}, ring thickness r/R, and eccentricity e. Each circle is colored by the highest net magnetization M/M_S corresponding to a local minimum of the total micromagnetic energy E_{tot} with red corresponding to single domain states, blue to vortex, and pale orange to intermediate onion states; the background color is interpolated between data points as a visual aid. The red and blue dashed lines indicate the boundaries from single domain to vortex states for configurations with the lowest E_{tot} (ground state), thus all nonvortex states at higher d_{tot} are metastable. The green circle, blue triangle, and red square mark approximate geometries of the green, blue, and red NPs measured by tomography in Figure 3.

agrees with experimental findings for nickel nanorings, which when normalized by exchange length (l_{ex}, a length scale intrinsic to materials below which behavior is dominated by atomic exchange interactions) predict the earliest onset of the vortex state at ~7 d_{tot}/l_{ex};[32] the exchange length for magnetite is approximately 9 nm and our phase diagram predicts vortex onset at 5.6−7.8 d_{tot}/l_{ex}. Therefore, toroidal magnetite NPs should be synthesized with a minimum diameter in this size region to ensure that the vortex state is accessible.

We observe that thin rings (low r/R) form vortex states at lower NP sizes than thick rings when considering the ground state configuration (dashed lines in Figure 2). This is intuitively understood by considering the impact of ring thickness at its limits: in thick toroids the cavity is negligible, and so uniform magnetization is preferred at small d_{tot}; in thin toroids, each segment is mostly polarized only by the segments ahead/behind, leading to radial vortex state magnetization. The opposite trend is observed for high M/M_S (metastable) states; thin rings are more likely to form the onion state even at high d_{tot} than an equivalent diameter thick ring. This seeming contradiction arises because thinner rings have a lower volume; findings by Einsle et al. suggest that NPs with greater volume have more stable vortex domains.[49] The balance of the thin-ring preference at low d_{tot} versus increased volume at high d_{tot} results in a diagonal protrusion of the vortex region (down and left from the main region, prominent for e = 0.7 in Figure 2). This "protrusion region" is attractive as a target NP geometry for combining stable vortex states and low diameter.

Particle eccentricity plays a large role in determining the final remanent state; high eccentricity shifts the ground state single domain/vortex boundary to lower NP diameters (Figure 2). This can also be attributed to the increased volume linked with high e. Another important effect of increased eccentricity is to decrease the stability of the onion state; the onion state has a net in-plane magnetization, so magnetic poles form on opposite faces of the NP, and these faces increase in area with

https://dx.doi.org/10.1021/acs.nanolett.0c02795
Nano Lett. XXXX, XXX, XXX−XXX

increasing eccentricity which is penalized by high energy contributions from shape anisotropy. This is pronounced at large r/R values which is why the metastable transition region spans only a short diameter range at high thickness and high eccentricity.

The initial magnetization used in the micromagnetic simulations impacts the final state because the outcome is naturally biased toward energy minima that resemble the initial configuration. This implies that metastable remanent states exist, separated by energy barriers. By comparing the initial state with the final phase diagram (SI Figure S7), we observe that uniform/random initial states will likely yield metastable onion states/stable vortex states, respectively. This has implications for how NPs are likely to behave in real-world applications, where NPs are typically left to relax following uniform magnetization in a large external field; observed remanent states are likely to correspond to reported high M/M_S states for low eccentricity NPs.

A major exception to this generalization occurs in the protrusion region where random initializations lead to higher energy states (SI Figure S7). Inspection of the exact structure of the randomly initialized $e = 0.9$ remanent states reveals that high M/M_S (metastable) states in the protrusion region from $d_{tot} = 70-110$ nm and $r/R = 0.2-0.4$ adopt a previously unreported "twisted onion state" similar to the onion state except that the z-component of magnetization twists from up to down as the xy component curls symmetrically around the NP (SI Figure S8). The twisted onion state was only found from random initializations, so we expect experimental conditions for highly eccentric NPs in this region to produce low E_{tot} configurations that are likely to be in the vortex state. This suggests that highly eccentric "tube" or "barrel" shaped NPs may be more suitable for biomedical applications.

The numerical values reported here are valid only for cubic, single-crystal magnetite with the [111] crystal axis aligned parallel to the particle z-axis as found experimentally.[13] However, these trends generalize to other single-crystalline materials by normalizing the ring diameter by the material exchange length and adjusting the saturation magnetization appropriately; other numerical and experimental studies found minimal impact of the orientation of the crystal axis on the magnetic behavior due to the overwhelming contribution from the demagnetization energy term.[13,28] However, the magnetocrystalline anisotropy plays a more dominant role in epitaxial rings, leading to distorted onion/vortex states;[50] further, polycrystalline rings are unable to form vortices at the same geometries as single-crystal rings.[51]

■ ELECTRON TOMOGRAPHY

Electron tomography allows the recording of the 3D structure of nanoscale NPs with high fidelity, ideal for studying toroidal NPs where geometry determines the magnetic state. We reconstructed a cluster of rings from a tilt series of 46 HAADF-STEM images using a compressed-sensing regularization algorithm[52−54] (Supporting Information). Intensity thresholding of the reconstructed volume was used to generate isosurfaces of three NPs for visualization (Figure 3), which were chosen because they were relatively unobscured by other particles, enabling higher fidelity reconstructions.

The volume reconstruction matches well with the real NP geometry (compare Figure 3 panels a and b with panel c). No beam damage or contamination was observed during acquisition (Figure 3a,b), permitting a high-quality reconstruction devoid of streaking and background signal, as seen in the orthoslices (Figure 3d). Isosurfaces were calibrated to within 1 nm precision and dimensions were measured for the green, blue, and red NPs, respectively, finding the following: average total diameters d_{tot}, 80 ± 5, 72 ± 4, and 61 ± 2 nm; average ring thickness r/R, 0.57 ± 0.03, 0.27 ± 0.07, and 0.41 ± 0.04; and average eccentricity e, 0.6 ± 0.1, 0.93 ± 0.03, and 0.69 ± 0.09. Each dimension is reported with its deviation when measured along eight diameters of the experimental toroid shapes (calculated according to ref. 55). Experimental shapes are well approximated by toroids as they have a mere 10% average deviation from toroidal geometry; imperfections include varying values of r and R around the toroids, eccentricity about the axis of rotation, and concavities/protrusions. The measured rings appear representative of other rings in the sample, although some particles without cavities were also observed; these particles are expected to behave similarly to spherical iron oxide NPs.[1]

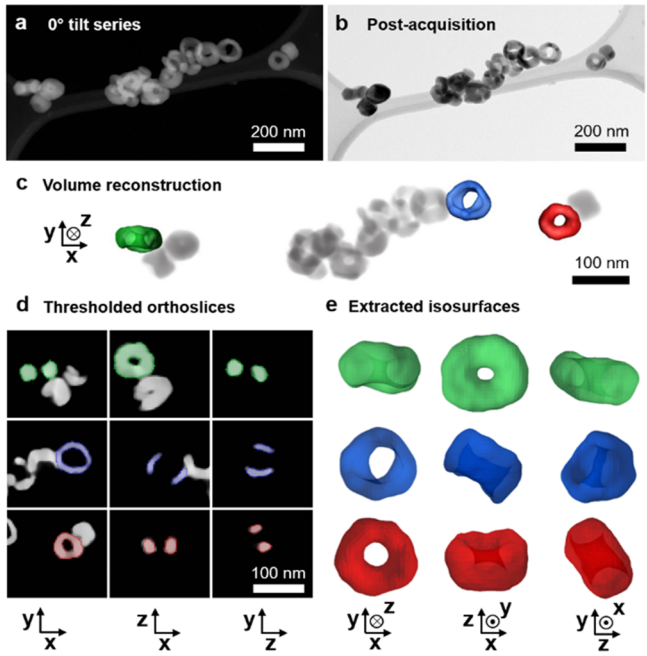

Figure 3. Tomographic reconstruction of nanorings. (a) HAADF-STEM 0° slice acquired during tomographic tilt series and (b) postacquisition bright-field TEM (BF-TEM). (c) Three-dimensional volume render generated by compressed sensing reconstruction with the three toroids highlighted in green, blue, and red. (d) Representative orthoslices with thresholding levels and (e) extracted isosurfaces for the highlighted NPs.

The experimental shapes represented by isosurfaces in Figure 3e were converted to tetrahedral volume meshes using constrained Delaunay tetrahedralization in the open source iso2mesh toolbox[56] and used as input for micromagnetic simulations in MERRILL.[47] Each ring was relaxed from x, y, and z initial uniform magnetizations to match experimental conditions. The results from the x initialization are shown in Figure 4; near-identical remanent states were found from y- and z-initializations (SI Figure S9).

The blue ring exists in a vortex state, while the green and red rings are essentially single domain. For the red and green NPs, this agrees well with the high M/M_S (metastable) phase diagram in Figure 2 on which the geometries of all three NPs are superimposed. Furthermore, calculation of remanent states

https://dx.doi.org/10.1021/acs.nanolett.0c02795
Nano Lett. XXXX, XXX, XXX−XXX

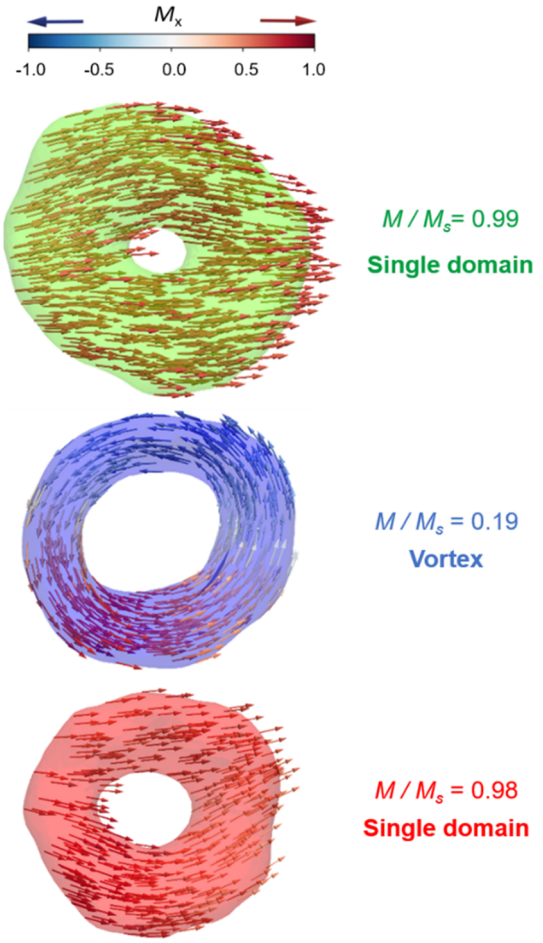

Figure 4. Tomography-based micromagnetic simulations. Calculated remanent states visualized for the green, blue, and red extracted ring geometries from Figure 3 for uniform *x*-magnetization initializations with corresponding net magnetization values and assigned magnetic state.

for extracted shapes at varying sizes (SI Figure S9) found that the boundary for vortex formation was 130 ± 20 and 100 ± 10 nm for the green and red rings, respectively, which matches the 125 and 105 nm boundaries from the high M/M_S (metastable) simulations. The highly eccentric blue ring, however, adopts the low E_{tot} ground state because its geometry falls into the protrusion region and its high eccentricity destabilizes the onion state. These results confirm that NPs with high eccentricity and thickness/diameter values in the protrusion region are likely to form vortex states and, importantly, that the micromagnetic phase diagram in Figure 2 is robust to small experimental variations in NP geometry.

IMPACT OF SHAPE IMPERFECTIONS

To further investigate the difference in magnetic behavior caused by geometric defects, shapes were generated by interpolating between the (ideal) toroids and the (real) tomography results. Using the open source software Blender, we projected each vertex on the ideal mesh along a line toward the closest neighboring surface point on the real mesh, and created shapes with vertices interpolated 0% (ideal shape), 20%, 40%, 60%, 80%, and 100% (real shape) along the line (Figure 5e). The Hausdorff distance[57] (maximum distance between a point on the interpolated shape to its closest neighbor in the ideal shape), computed in Meshlab,[58] was used as a measure of shape deviation encompassing all types of imperfection. Several tests of magnetic behavior were carried out on these interpolated shapes: the net magnetization of the remanent vortex state was found by relaxing from random initial states; the stray field associated with each vortex state was averaged over a 300 nm × 300 nm area centered on the NP, after projecting the particle magnetization into 2D parallel to the *z*-axis; and energy barriers between onion and vortex states were calculated using a nudged elastic band algorithm[59,60] implemented in MERRILL[47] (Supporting Information).

As the Hausdorff distance increases, the net magnetization (Figure 5a) and stray field (Figure 5b) increase, indicating a lower quality vortex state. The type of imperfection impacts the magnitude of this effect; the green ring has an ∼7 nm lateral compression in the plane of the ring but is mostly free from large bumps or notches, giving a smaller Hausdorff distance and overall lower increase in M/M_S and stray field compared to the blue and red rings. The blue ring has a significant ∼10 nm notch on one side, whereas the red ring has two ∼8 nm bumps on diagonally opposite edges; these have a large impact on vortex quality with increases in both net magnetization and stray field. The blue ring shows a particularly large increase in net magnetization due to the asymmetry of its defects, while the red ring exhibits a steep increase in stray field as the two bumps act as stray field sources, as demonstrated by Williams et al.[37] Note that the nonzero Hausdorff distance in the 0% interpolated shapes is a minor numerical artifact due to the finite resolution of the tetrahedral meshes.

The energy barrier to reconfiguration between onion and vortex states increases with deviation from ideal geometry for green and red rings; however, the blue ring shows a decreasing trend, suggesting the vortex state forms more easily with the defects present (Figure 5c). Along the transition pathway, we see for the blue ring that the initial onion state is asymmetric, and the magnetization rotates out-of-plane only in the thin notched region causing a modest increase in demagnetization energy (SI Figure S10). For the green and red rings, the initial onion state is much more uniformly magnetized, and the out-of-plane rotation is forced to take place over a wide section of the ring, incurring a large demagnetization energy penalty. This suggests that rings with varying thickness around their perimeter may actually be advantageous in making the vortex state more accessible which is in agreement with similar conclusions for off-centered rings.[28]

The key utility of the vortex state is to avoid dipolar coupling between adjacent particles, leading to stable dispersions. We probed this interaction by calculating the net magnetization for a two-particle system with one ring at the origin and the other displaced along the *x*-axis, initially uniformly magnetized parallel to *x*. This state is the least favorable for minimizing magnetic interaction[28] and leads to an upper bound on the required separation distance. The second particle was rotated parallel to its central axis by 0°, 90°, 180°, and 270° with results averaged to avoid orientation bias. We found for the blue ring that despite the significantly higher net magnetization of the real versus ideal particle, dipolar coupling merely increases the separation distance required for vortex formation by 1 nm, from 2 nm (ideal toroid) to 3 nm (Figure 5d). This is a negligible change in performance considering that NPs are typically coated in a surfactant layer up to 8 nm thick.[20] Such a

https://dx.doi.org/10.1021/acs.nanolett.0c02795
Nano Lett. XXXX, XXX, XXX−XXX

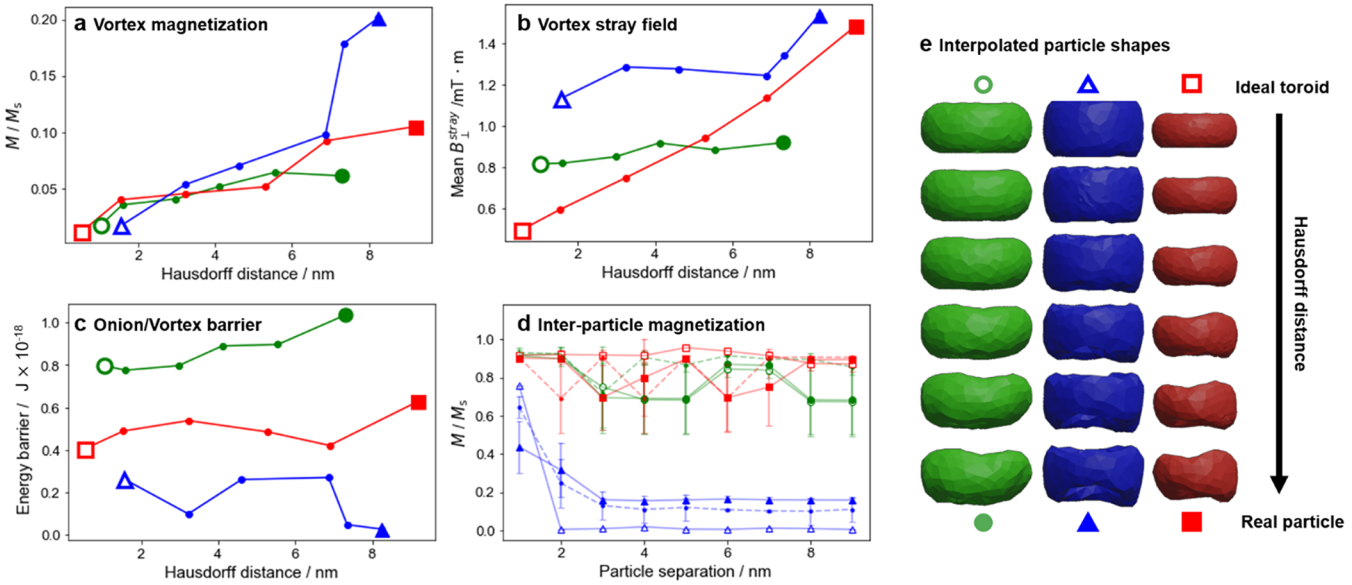

Figure 5. Impact of shape imperfections on magnetic behavior. (a) Calculated net magnetization of the vortex remanent state for interpolated particles. (b) Simulated stray field, $B_{\perp}^{stray}$ averaged over a 300 nm × 300 nm area perpendicular to the central axis of each particle after projection along the central axis. (c) Energy barrier between the onion and vortex states calculated using a nudged elastic band algorithm. (d) Calculated net magnetization for a two-particle system, initially magnetized parallel to the *x*-axis and the second particle displaced along the *x*-axis; error bars are calculated as the standard error on four simulations at each point, corresponding to the second particle being rotated parallel to its central axis by 0°, 90°, 180°, or 270°. The dashed lines correspond to the geometries interpolated 60% between real and ideal. (e) Illustration of the analyzed particle geometries, interpolated between the ideal toroid shape and the "real" tomography-extracted shape. Ideal/real geometries are represented by an open/closed circle, triangle, and square for the green, blue, and red rings, respectively.

coating prevents the possibility of direct exchange interactions and significantly decreases the potency of dipolar coupling.[61] As expected from the results in Figure 4, the red and green particles remain magnetized in an onion state over all separation distances.

CONCLUSIONS

We produced a magnetic phase diagram predicting toroidal geometries that sustain a magnetic vortex remanent state in magnetite with thin-ringed, eccentric tubular NPs having stable vortex states at the lowest NP diameters, down to a minimum diameter of ∼60 nm. These findings also suggest that all toroidal NPs at sizes above the low E_{tot} transition boundary could be converted into the vortex state from other metastable states if given sufficient energy to overcome the reconfiguration barrier.

By utilizing the real particle shapes extracted by electron tomography, we showed that shape imperfections can lead to an increase in the stray field, and in some cases make the vortex state more energetically accessible. These defects are unlikely to compromise dispersion stability so long as a particle separation of more than 3 nm is maintained by surface layers. Combined with the phase diagram results, this suggests that the overall geometrical parameters of the ring (diameter, thickness, and eccentricity) play a much bigger role in determining the remanent state than particle defects. These results constitute an important step toward the rational tuning of toroidal nanoparticles to the vortex state that is key for potential biomedical applications and is responsible for their unique behavior.

ASSOCIATED CONTENT

Supporting Information

The Supporting Information is available free of charge at https://pubs.acs.org/doi/10.1021/acs.nanolett.0c02795.

Supplementary text and figures including hysteresis loops, iron oxide crystallinity, NP geometry, additional simulations, and additional details on methods (PDF)

AUTHOR INFORMATION

Corresponding Author

Emilie Ringe − *Department of Materials Science and Metallurgy and Department of Earth Sciences, University of Cambridge, Cambridge CB3 0FS, United Kingdom;* orcid.org/0000-0003-3743-9204; Email: er407@cam.ac.uk

Authors

George R. Lewis − *Department of Materials Science and Metallurgy and Department of Earth Sciences, University of Cambridge, Cambridge CB3 0FS, United Kingdom;* orcid.org/0000-0001-9232-4253

James C. Loudon − *Department of Materials Science and Metallurgy, University of Cambridge, Cambridge CB3 0FS, United Kingdom*

Robert Tovey − *Department of Applied Mathematics and Theoretical Physics, University of Cambridge, Cambridge CB3 0WA, United Kingdom*

Yen-Hua Chen − *Department of Earth Sciences, National Cheng Kung University, Tainan 70101, Taiwan*

Andrew P. Roberts − *Research School of Earth Sciences, The Australian National University, Canberra, Australian Capital Territory 2601, Australia*

Richard J. Harrison − *Department of Earth Sciences, University of Cambridge, Cambridge CB2 3EQ, United Kingdom*

https://dx.doi.org/10.1021/acs.nanolett.0c02795
Nano Lett. XXXX, XXX, XXX−XXX

Paul A. Midgley − *Department of Materials Science and Metallurgy, University of Cambridge, Cambridge CB3 0FS, United Kingdom*

Complete contact information is available at: https://pubs.acs.org/10.1021/acs.nanolett.0c02795

Notes

The authors declare no competing financial interest.

■ ACKNOWLEDGMENTS

G.R.L. is thankful for support from the EPSRC NanoDTC Cambridge (No. EP/L015978/1). R.T. acknowledges funding from EPSRC Grant EP/L016516/1 for the Cambridge Centre for Analysis, and the Cantab Capital Institute for the Mathematics of Information. P.A.M. thanks the EPSRC for financial support under Grant EP/R008779/1. A.P.R. and R.J.H. acknowledge funding from the Australian Research Council (grant DP200100765). E.R. acknowledges Trinity College Dublin's Visiting Professor Fund. We would like to thank Lewys Jones and Clive Downing at the CRANN Advanced Microscopy Laboratory for acquiring EDX data (SFI Grant AMBER2-12/RC/2278_P2). We would also like to thank Dr Xiang Zhao at ANU for acquiring FORC data.

■ REFERENCES

(1) Laurent, S.; Forge, D.; Port, M.; Roch, A.; Robic, C.; Vander Elst, L.; Muller, R. N. Magnetic Iron Oxide Nanoparticles: Synthesis, Stabilization, Vectorization, Physicochemical Characterizations, and Biological Applications. *Chem. Rev.* **2008**, *108* (6), 2064−2110.

(2) Pankhurst, Q. A.; Connolly, J.; Jones, S. K.; Dobson, J. Applications of Magnetic Nanoparticles in Biomedicine. *J. Phys. D: Appl. Phys.* **2003**, *36* (13), R167−R181.

(3) Lu, A.-H.; Salabas, E. L.; Schüth, F. Magnetic Nanoparticles: Synthesis, Protection, Functionalization, and Application. *Angew. Chem., Int. Ed.* **2007**, *46* (8), 1222−1244.

(4) Cornell, R. M.; Schwertmann, U. *The Iron Oxides: Structure, Properties, Reactions, Occurences and Uses*, 2nd ed.; Wiley-VCH Verlag GmbH & Co. KGaA: Weinheim, 2003.

(5) Chang, D.; Lim, M.; Goos, J. A. C. M.; Qiao, R.; Ng, Y. Y.; Mansfeld, F. M.; Jackson, M.; Davis, T. P.; Kavallaris, M. Biologically Targeted Magnetic Hyperthermia: Potential and Limitations. *Front. Pharmacol.* **2018**, *9*, 831.

(6) Fortin, J. P.; Wilhelm, C.; Servais, J.; Ménager, C.; Bacri, J. C.; Gazeau, F. Size-Sorted Anionic Iron Oxide Nanomagnets as Colloidal Mediators for Magnetic Hyperthermia. *J. Am. Chem. Soc.* **2007**, *129* (9), 2628−2635.

(7) Vangijzegem, T.; Stanicki, D.; Laurent, S. Magnetic Iron Oxide Nanoparticles for Drug Delivery: Applications and Characteristics. *Expert Opin. Drug Delivery* **2019**, *16*, 69−78.

(8) Hola, K.; Markova, Z.; Zoppellaro, G.; Tucek, J.; Zboril, R. Tailored Functionalization of Iron Oxide Nanoparticles for MRI, Drug Delivery, Magnetic Separation and Immobilization of Biosubstances. *Biotechnol. Adv.* **2015**, *33*, 1162−1176.

(9) Abenojar, E. C.; Wickramasinghe, S.; Bas-Concepcion, J.; Samia, A. C. S. Structural Effects on the Magnetic Hyperthermia Properties of Iron Oxide Nanoparticles. *Prog. Nat. Sci.* **2016**, *26*, 440−448.

(10) Kloust, H.; Zierold, R.; Merkl, J.-P.; Schmidtke, C.; Feld, A.; Poselt, E.; Kornowski, A.; Nielsch, K.; Weller, H. Synthesis of Iron Oxide Nanorods Using a Template Mediated Approach. *Chem. Mater.* **2015**, *27*, 4914−4917.

(11) Islam, M. S.; Kusumoto, Y.; Abdulla-Al-Mamun, M. Novel Rose-Type Magnetic (Fe3O4, γ-Fe2O3 and α-Fe2O3) Nanoplates Synthesized by Simple Hydrothermal Decomposition. *Mater. Lett.* **2012**, *66*, 165−167.

(12) De Montferrand, C.; Hu, L.; Milosevic, I.; Russier, V.; Bonnin, D.; Motte, L.; Brioude, A.; Lalatonne, Y. Iron Oxide Nanoparticles with Sizes, Shapes and Compositions Resulting in Different Magnetization Signatures as Potential Labels for Multiparametric Detection. *Acta Biomater.* **2013**, *9*, 6150−6157.

(13) Jia, C.-J.; Sun, L.-D.; Luo, F.; Han, X.-D.; Heyderman, L. J.; Yan, Z.-G.; Yan, C.-H.; Zheng, K.; Zhang, Z.; Takano, M.; et al. Large-Scale Synthesis of Single-Crystalline Iron Oxide Magnetic Nanorings. *J. Am. Chem. Soc.* **2008**, *130* (50), 16968−16977.

(14) Fan, H. M.; Yi, J. B.; Yang, Y.; Kho, K. W.; Tan, H. R.; Shen, Z. X.; Ding, J.; Sun, X. W.; Olivo, M. C.; Feng, Y. P. Single-Crystalline MFe2O4 Nanotubes/Nanorings Synthesized by Thermal Transformation Process for Biological Applications. *ACS Nano* **2009**, *3* (9), 2798−2808.

(15) Shinjo, T.; Okuno, T.; Hassdorf, R.; Shigeto, K.; Ono, T. Magnetic Vortex Core Observation in Circular Dots of Permalloy. *Science* **2000**, *289* (5481), 930−932.

(16) Huo, Y.; Zhu, Y.; Xie, J.; Cao, G.; Zhu, T.; Zhao, X.; Zhang, S. Controllable Synthesis of Hollow α-Fe2O3 Nanostructures, Their Growth Mechanism, and the Morphology-Reserved Conversion to Magnetic Fe3O4/C Nanocomposites. *RSC Adv.* **2013**, *3*, 19097−19103.

(17) Liu, X.-L.; Yang, Y.; Wu, J.-P.; Zhang, Y.-F.; Fan, H.-M.; Ding, J. Novel Magnetic Vortex Nanorings/Nanodiscs: Synthesis and Theranostic Applications. *Chin. Phys. B* **2015**, *24* (12), 127505.

(18) Dias, C. S. B.; Hanchuk, T. D. M.; Wender, H.; Shigeyosi, W. T.; Kobarg, J.; Rossi, A. L.; Tanaka, M. N.; Cardoso, M. B.; Garcia, F. Shape Tailored Magnetic Nanorings for Intracellular Hyperthermia Cancer Therapy. *Sci. Rep.* **2017**, *7*, 14843.

(19) Liu, X.; Zheng, J.; Sun, W.; Zhao, X.; Li, Y.; Gong, N.; Wang, Y.; Ma, X.; Zhang, T.; Zhao, L.-Y.; et al. Ferrimagnetic Vortex Nanoring-Mediated Mild Magnetic Hyperthermia Imparts Potent Immunological Effect for Treating Cancer Metastasis. *ACS Nano* **2019**, *13* (8), 8811−8825.

(20) Liu, X. L.; Yang, Y.; Ng, C. T.; Zhao, L. Y.; Zhang, Y.; Bay, B. H.; Fan, H. M.; Ding, J. Magnetic Vortex Nanorings: A New Class of Hyperthermia Agent for Highly Efficient In Vivo Regression of Tumors. *Adv. Mater.* **2015**, *27*, 1939−1944.

(21) Liu, X.; Peng, M.; Li, G.; Miao, Y.; Luo, H.; Jing, G.; He, Y.; Zhang, C.; Zhang, F.; Fan, H. Ultrasonication-Triggered Ubiquitous Assembly of Magnetic Janus Amphiphilic Nanoparticles in Cancer Theranostic Applications. *Nano Lett.* **2019**, *19*, 4118−4125.

(22) Liu, X.; Yan, B.; Li, Y.; Ma, X.; Jiao, W.; Shi, K.; Zhang, T.; Chen, S.; He, Y.; Liang, X.-J.; et al. Graphene Oxide-Grafted Magnetic Nanorings Mediated Magnetothermodynamic Therapy Favoring Reactive Oxygen Species-Related Immune Response for Enhanced Antitumor Efficacy. *ACS Nano* **2020**, *14* (2), 1936−1950.

(23) Yan, X.; Wu, Y.; Li, D.; Luo, C.; Wang, Y.; Hu, J.; Li, G.; Li, P.; Jiang, H.; Zhang, W. Facile Synthesis of Ring-like α-Fe2O3 Assembly Composed of Small Hematite Particles for Highly Efficient Photocatalysis. *J. Mater. Sci.: Mater. Electron.* **2018**, *29*, 2610−2617.

(24) Lee, K. S.; Park, S.; Lee, W.; Yoon, Y. S. Hollow Nanobarrels of α-Fe2O3 on Reduced Graphene Oxide as High-Performance Anode for Lithium-Ion Batteries. *ACS Appl. Mater. Interfaces* **2016**, *8*, 2027−2034.

(25) Ding, Y.; Zhang, L.; Liao, Q.; Zhang, G.; Liu, S.; Zhang, Y. Electromagnetic Wave Absorption in Reduced Graphene Oxide Functionalized with Fe3O4/Fe Nanorings. *Nano Res.* **2016**, *9* (7), 2018−2025.

(26) Fan, H. M.; Olivo, M.; Shuter, B.; Yi, J. B.; Bhuvaneswari, R.; Tan, H. R.; Xing, G. C.; Ng, C. T.; Liu, L.; Lucky, S. S.; et al. Quantum Dot Capped Magnetite Nanorings as High Performance Nanoprobe for Multiphoton Fluorescence and Magnetic Resonance Imaging. *J. Am. Chem. Soc.* **2010**, *132* (42), 14803−14811.

(27) Rothman, J.; Kläui, M.; Lopez-Diaz, L.; Vaz, C. A. F. F.; Bleloch, A.; Bland, J. A. C.; Cui, Z.; Speaks, R. Observation of a Bi-Domain State and Nucleation Free Switching in Mesoscopic Ring Magnets. *Phys. Rev. Lett.* **2001**, *86* (6), 1098−1101.

(28) Yang, Y.; Liu, X.-L.; Yi, J.-B.; Yang, Y.; Fan, H.-M.; Ding, J. Stable Vortex Magnetite Nanorings Colloid: Micromagnetic Simu-

lation and Experimental Demonstration. *J. Appl. Phys.* **2012**, *111*, 044303.
(29) Kläui, M.; Vaz, C. A. F.; Heyderman, L. J.; Rüdiger, U.; Bland, J. A. C. Spin Switching Phase Diagram of Mesoscopic Ring Magnets. *J. Magn. Magn. Mater.* **2005**, *290*−*291*, 61−67.
(30) Benatmane, N.; Scholz, W.; Clinton, T. W. Magnetic Configurations and Phase Diagrams of Sub-100-Nm NiFe Nanorings. *IEEE Trans. Magn.* **2007**, *43* (6), 2884−2886.
(31) Chung, S.-H.; McMichael, R. D.; Pierce, D. T.; Unguris, J. Phase Diagram of Magnetic Nanodisks Measured by Scanning Electron Microscopy with Polarization Analysis. *Phys. Rev. B: Condens. Matter Mater. Phys.* **2010**, *81* (2), 024410.
(32) Scholz, W.; Guslienko, K. Y.; Novosad, V.; Suess, D.; Schrefl, T.; Chantrell, R. W.; Fidler, J. Transition from Single-Domain to Vortex State in Soft Magnetic Cylindrical Nanodots. *J. Magn. Magn. Mater.* **2003**, *266*, 155−163.
(33) Gregurec, D.; Senko, A. W.; Chuvilin, A.; Reddy, P. D.; Sankararaman, A.; Rosenfeld, D.; Chiang, P.-H.; Garcia, F.; Tafel, I.; Varnavides, G.; Ciocan, E.; Anikeeva, P. Magnetic Vortex Nanodiscs Enable Remote Magnetomechanical Neural Stimulation. *ACS Nano* **2020**, *14*, 8036.
(34) Gao, H.-X.; Zhang, T.; Zhang, Y.; Chen, Y. M.; Liu, B.; Wu, J.; Liu, X. L.; Li, Y.; Peng, M.; Zhang, Y.; et al. Ellipsoidal Magnetite Nanoparticles: A New Member of Magnetic-Vortex Nanoparticles Family for Efficient Magnetic Hyperthermia. *J. Mater. Chem. B* **2020**, *8*, 515−522.
(35) Cambel, V.; Karapetrov, G. Control of Vortex Chirality and Polarity in Magnetic Nanodots with Broken Rotational Symmetry. *Phys. Rev. B: Condens. Matter Mater. Phys.* **2011**, *84*, 14424.
(36) He, K.; Smith, D. J.; Mccartney, M. R. Effects of Vortex Chirality and Shape Anisotropy on Magnetization Reversal of Co Nanorings (Invited). *J. Appl. Phys.* **2010**, *107* (9), 09D307.
(37) Williams, W.; Muxworthy, A. R.; Evans, M. E. A Micromagnetic Investigation of Magnetite Grains in the Form of Platonic Polyhedra with Surface Roughness. *Geochem., Geophys., Geosyst.* **2011**, *12* (10), Q10Z31.
(38) Eltschka, M.; Kläui, M.; Rüdiger, U.; Kasama, T.; Cervera-Gontard, L.; Dunin-Borkowski, R. E.; Luo, F.; Heyderman, L. J.; Jia, C.-J.; Sun, L.-D.; et al. Correlation between Magnetic Spin Structure and the Three-Dimensional Geometry in Chemically Synthesized Nanoscale Magnetite Rings. *Appl. Phys. Lett.* **2008**, *92*, 222508.
(39) Kläui, M.; Vaz, C. A. F.; Lopez-Diaz, L.; Bland, J. A. C. Vortex Formation in Narrow Ferromagnetic Rings. *J. Phys.: Condens. Matter* **2003**, *15*, R985−R1203.
(40) Park, M. H.; Hong, Y. K.; Choi, B. C.; Donahue, M. J.; Han, H.; Gee, S. H. Vortex Head-to-Head Domain Walls and Their Formation in Onion-State Ring Elements. *Phys. Rev. B: Condens. Matter Mater. Phys.* **2006**, *73* (9), 094424.
(41) Hu, J.-M.; Yang, T.; Momeni, K.; Cheng, X.; Chen, L.; Lei, S.; Zhang, S.; Trolier-McKinstry, S.; Gopalan, V.; Carman, G. P.; et al. Fast Magnetic Domain-Wall Motion in a Ring-Shaped Nanowire Driven by a Voltage. *Nano Lett.* **2016**, *16*, 2341−2348.
(42) Ehrmann, A.; Blachowicz, T. Magnetization Reversal in Ferromagnetic Nanorings of Fourfold Symmetries. *Adv. Mater. Sci. Eng.* **2017**, *2017*, 1−7.
(43) Mu, C.; Jing, J.; Dong, J.; Wang, W.; Xu, J.; Nie, A.; Xiang, J.; Wen, F.; Liu, Z. Static and Dynamic Characteristics of Magnetism in Permalloy Oval Nanoring by Micromagnetic Simulation. *J. Magn. Magn. Mater.* **2019**, *474*, 301−304.
(44) Chen, Y. H.; Lin, C. C. Effect of Nano-Hematite Morphology on Photocatalytic Activity. *Phys. Chem. Miner.* **2014**, *41*, 727−736.
(45) Hu, P.; Zhang, S.; Wang, H.; Pan, D.; Tian, J.; Tang, Z.; Volinsky, A. A. Heat Treatment Effects on Fe3O4 Nanoparticles Structure and Magnetic Properties Prepared by Carbothermal Reduction. *J. Alloys Compd.* **2011**, *509*, 2316−2319.
(46) Widdrat, M.; Kumari, M.; Tompa, É.; Pósfai, M.; Hirt, A. M.; Faivre, D. Keeping Nanoparticles Fully Functional: Long-Term Storage and Alteration of Magnetite. *ChemPlusChem* **2014**, *79* (8), 1225−1233.
(47) Conbhui, P. O.; Williams, W.; Fabian, K.; Ridley, P.; Nagy, L.; Muxworthy, A. R. MERRILL: Micromagnetic Earth Related Robust Interpreted Language Laboratory. *Geochem., Geophys., Geosyst.* **2018**, *19*, 1080−1106.
(48) Muxworthy, A. R.; Williams, W. Critical Single-Domain Grain Sizes in Elongated Iron Particles: Implications for Meteoritic and Lunar Magnetism. *Geophys. J. Int.* **2015**, *202*, 578−583.
(49) Einsle, J. F.; Harrison, R. J.; Kasama, T.; Conbhuí, P.; Fabian, K.; Williams, W.; Woodland, L.; Fu, R. R.; Weiss, B. P.; Midgley, P. A. Multi-Scale Three-Dimensional Characterization of Iron Particles in Dusty Olivine: Implications for Paleomagnetism of Chondritic Meteorites. *Am. Mineral.* **2016**, *101* (9), 2070−2084.
(50) Fonin, M.; Hartung, C.; Rüdiger, U.; Backes, D.; Heyderman, L.; Nolting, F.; Rodríguez, A. F.; Kläui, M. Formation of Magnetic Domains and Domain Walls in Epitaxial Fe 3 O 4 (100) Elements (Invited). *J. Appl. Phys.* **2011**, *109* (7), 07D315.
(51) Das, R.; Witanachchi, C.; Nemati, Z.; Kalappattil, V.; Rodrigo, I.; García, J. A.; Garaio, E.; Alonso, J.; Lam, V. D.; Le, A.-T.; et al. Magnetic Vortex and Hyperthermia Suppression in Multigrain Iron Oxide Nanorings. *Appl. Sci.* **2020**, *10* (3), 787.
(52) Goris, B.; Van den Broek, W.; Batenburg, K. J.; Heidari Mezerji, H.; Bals, S. Electron Tomography Based on a Total Variation Minimization Reconstruction Technique. *Ultramicroscopy* **2012**, *113*, 120−130.
(53) Chambolle, A.; Pock, T. A First-Order Primal-Dual Algorithm for Convex Problems with Applications to Imaging. *J. Math. Imaging Vis.* **2011**, *40* (1), 120−145.
(54) Leary, R.; Saghi, Z.; Midgley, P. A.; Holland, D. J. Compressed Sensing Electron Tomography. *Ultramicroscopy* **2013**, *131*, 70−91.
(55) Hughes, I. G.; Hase, T. P. A. *Measurements and Their Uncertainties*; Oxford University Press: Oxford, 2010.
(56) Fang, Q.; Boas, D. A. Tetrahedral Mesh Generation from Volumetric Binary and Gray-Scale Images. In *2009 IEEE International Symposium on Biomedical Imaging: From Nano to Macro*; Boston, 2009; pp 1142−1145.
(57) Cignoni, P.; Rocchini, C.; Scopigno, R. Metro: Measuring Error on Simplified Surfaces. *Comput. Graph. Forum* **1998**, *17* (2), 167−174.
(58) Cignoni, P.; Callieri, M.; Corsini, M.; Dellepiane, M.; Ganovelli, F.; Ranzuglia, G. MeshLab: An Open-Source Mesh Processing Tool. *Sixth Eurographics Ital. Chapter Conf.*, Salerno, Italy, July 2nd - 4th, 2008, 129136.
(59) Henkelman, G.; Jónsson, H. Improved Tangent Estimate in the Nudged Elastic Band Method for Finding Minimum Energy Paths and Saddle Points. *J. Chem. Phys.* **2000**, *113* (22), 9978−9985.
(60) Dittrich, R.; Schrefl, T.; Suess, D.; Scholz, W.; Forster, H.; Fidler, J. A Path Method for Finding Energy Barriers and Minimum Energy Paths in Complex Micromagnetic Systems. *J. Magn. Magn. Mater.* **2002**, *250*, 12−19.
(61) Usov, N. A.; Serebryakova, O. N.; Tarasov, V. P. Interaction Effects in Assembly of Magnetic Nanoparticles. *Nanoscale Res. Lett.* **2017**, *12* (1), 1−8.

https://dx.doi.org/10.1021/acs.nanolett.0c02795
Nano Lett. XXXX, XXX, XXX−XXX